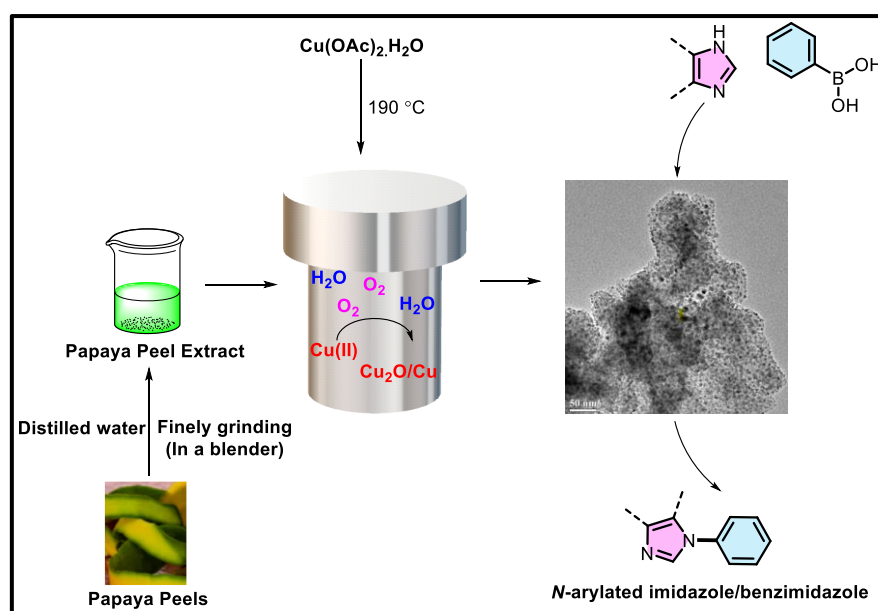


# Chapter 5

## Biogenic Cu<sub>2</sub>O/Cu Nanomaterial Catalysed *N*-arylation of Imidazoles and Benzimidazoles with Arylboronic acids Under External Base Free Conditions



**Abstract:** A cost-effective and eco-friendly method to synthesise copper nanoparticles (NPs) using agro-waste materials is presented by us. This method involves *in-situ* fabrication of Cu<sub>2</sub>O particles on copper surfaces through gas-phase H<sub>2</sub>O/O<sub>2</sub> stimulation, eliminating the need for conventional reducing agents. The Cu<sub>2</sub>O/Cu NPs obtained are highly efficient in catalysing the synthesis of *N*-arylated imidazole and benzimidazole derivatives. The catalytic activity arises from the synergy between Cu(0) and Cu(I) surfaces, enabling effective C–C and C–N coupling reactions with arylboronic acids. Moreover, the catalyst is reusable, maintaining its efficiency across multiple cycles with minimal performance degradation.

---

### Biogenic Cu<sub>2</sub>O/Cu Nanomaterial Catalysed *N*-arylation of Imidazoles and Benzimidazoles with Arylboronic acids Under External Base Free Conditions

#### 5.1. Introduction

Metal nanoparticles (NPs) have emerged as invaluable resources in catalysis, enabling a vast array of chemical transformations critical to industrial applications [1, 2]. Among these, palladium nanoparticles (Pd NPs) have garnered significant attention for their superior catalytic activity and selectivity in cross-coupling reactions, making them indispensable in organic synthesis despite their higher cost and limited availability. Complementing this, copper (Cu) nanoparticles, along with their oxide forms, stand out due to copper's high natural abundance, affordability, and adaptability in terms of morphology and crystalline structure. These features, combined with its monodispersed crystal structures, make Cu NPs highly sought after in catalysis. Importantly, the catalytic efficiency of Cu NPs is intricately tied to their morphology, which directly impacts their physical and chemical properties. As a result, extensive work was dedicated to the controlled synthesis of Cu NPs with various oxidation states, aiming to create a diverse range of morphologies sui for numerous applications [3, 4].

Researchers have explored and developed a wide variety of Cu-based nanoparticles and nanocrystals to evaluate their potential across different domains. Notably, their catalytic prowess in facilitating cross-coupling reactions has gained particular attention as it opens new pathways in organic synthesis. Cross-coupling reactions, such as the Ullmann [5], Sonogashira [6], Suzuki [7], Buchwald-Hartwig [8], and Chan-Lam reactions [9], catalysed by Cu- or Pd-based systems, are instrumental in producing intermediates vital for pharmaceuticals, biologically active compounds, materials chemistry, and beyond. The Ullmann reaction, a pioneering method for C–N bond formation, has been widely used for constructing aryl amines [5]. Traditionally requiring elevated temperatures and stoichiometric amounts of copper, it has been significantly improved in modern systems by employing ligands and optimised catalysts that enable milder, more sustainable reaction conditions. This reaction remains a cornerstone in synthetic organic chemistry, facilitating the

synthesis of dyes, pharmaceuticals, and polymers. Advances in hybrid Cu nanocatalysts have further enhanced the Ullmann reaction by offering improved catalytic activity, substrate scope, and reusability, thereby increasing its applicability in both academic and industrial settings [10].

Another critical tool for C–N bond formation is the Buchwald-Hartwig amination [8], which employs palladium-based catalysts to couple aryl halides with amines under gentler settings. This reaction is highly versatile, delivering a broad range of *N*-aryl and *N*-alkyl products with excellent functional group tolerance. It has become a workhorse in medicinal and materials chemistry due to its ability to generate diverse nitrogen-containing compounds. Recent innovations, such as the development of air-stable catalysts and ligands, have expanded the reaction's utility, making it more practical and scalable [11, 12, 13, 14]. Furthermore, the potential to combine palladium and copper systems has created synergistic effects that improve the efficiency of certain C–N coupling reactions [15]. The Chan-Lam reaction, a copper-catalysed C–N cross-coupling method, is particularly valued for its mild and environmentally friendly conditions. It involves the coupling of amines, imidazoles, or benzimidazoles with arylboronic acids, providing a reliable and efficient method for synthesising *N*-aryl functionalities. Introduced by D. Chan, D. Evans, and P. Lam, this reaction has evolved into a versatile tool in organic synthesis, especially in medicinal chemistry and agrochemical development [16, 17]. Unlike many other coupling reactions, the Chan-Lam reaction often proceeds under ambient or near-ambient conditions, reducing energy consumption and minimising the need for specialised equipment.

Furthermore, the reaction's compatibility with air and moisture eliminates the need for inert atmosphere setups, making it practical for large-scale operations. Its wide substrate scope allows for the functionalisation of complex molecules, enabling the synthesis of bioactive compounds, agrochemicals, and advanced materials. Hybrid Cu nanocatalysts have played a significant role in advancing the Chan-Lam reaction, offering enhanced activity, selectivity, and reusability. The dynamic interplay between Cu(0) and Cu(I) species in these systems improves reaction efficiency, broadening the substrate scope and product yield [18, 19, 20]. Herein, we aimed to develop an eco-friendly solvothermal approach for synthesising hybrid Cu NPs,

achieving controlled *in-situ* Cu<sub>2</sub>O formation using a water extract of papaya peels. Cu<sub>2</sub>O/Cu NPs formed in this method have demonstrated high catalytic activity in Chan–Lam type arylation of imidazoles and benzimidazoles with arylboronic acids. Both phases experience reversible oxidation and the transfer of electrons between the copper and copper (I) oxide surfaces leads to increased efficiency of the system [21].

### 5.2. Experimental Section

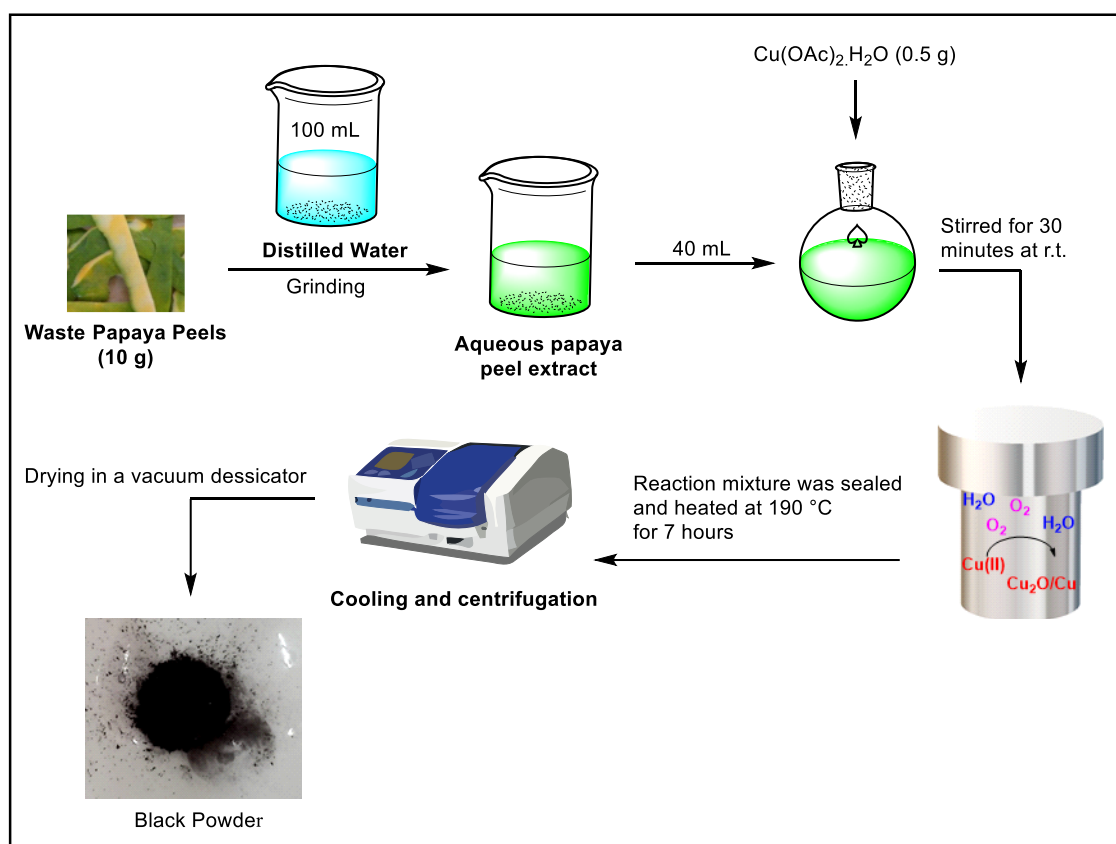
#### 5.2.1. Fabrication of the nanomaterial

Waste papaya peels (10 g) were rinsed with distilled water, finely chopped, and ground in 100 mL of distilled water. The extract was filtered using a sintered glass crucible and stored. Then, 0.5 g of copper acetate was mixed with 40 mL of the papaya peel extract in a 100 mL Teflon-lined stainless-steel autoclave. The mixture was stirred for 30 minutes to ensure a homogeneous solution of and extract. Finally, the sealed autoclave was heated to 463 K (190 °C) for 7 hours to obtain a black residue. The residue was separated using centrifugation followed by washing several times with distilled water and methanol. Subsequent drying using a vacuum desiccator resulted in the required material (Cu<sub>2</sub>O/Cu) (**Scheme 5.1**).

#### 5.2.2. Characterisation techniques

The fabricated copper nanomaterial was characterised by several analytical techniques to ensure comprehensive analysis of their structure and properties. Solid-state UV/Vis spectra, covering the 200-900 nm range, were obtained using a JASCO V-750 spectrophotometer, while infrared (IR) spectra were recorded on a Perkin Elmer Frontier MIR FIR FTIR spectrophotometer. The Powder XRD pattern of the samples was examined through X-ray diffraction (XRD) using a Rigaku MultiFlex instrument with a nickel-filtered Cu K $\alpha$  radiation source (0.15418 nm). For surface chemical analysis, X-ray photoelectron spectroscopy (XPS) measurements were conducted on a Thermo-Scientific ESCALAB Xi+ spectrometer, employing a monochromatic Al K $\alpha$  X-ray source (1486.6 eV) and a spherical energy analyser in constant analyser energy (CAE) mode, set at 100 eV for survey spectra and 50 eV for high-resolution spectra. Scanning electron microscopy (SEM) was performed using a JEOL JSM Model 6390 LV scanning electron microscope at an accelerating voltage of 15 kV, along with energy

dispersive X-ray (EDX) analysis to confirm the catalyst's elemental composition. Transmission electron microscopy (TEM) images were captured using a JEOL JEM-2010 instrument, offering further insight into the material's microstructure. Progress of the organic reactions carried out were monitored using silica gel 60-F254 coated on aluminium plates purchased from Merck and the TLC plates were visualised using iodine and UV lamp. Finally,  $^1\text{H}$  and  $^{13}\text{C}$  NMR spectra were recorded on a Jeol ECS 400 MHz NMR spectrophotometer (JEOL) with tetramethylsilane (TMS) as an internal standard.

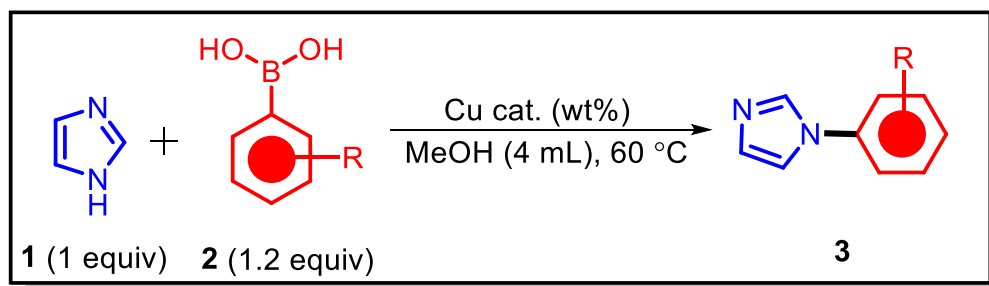


**Scheme 5.1.** Fabrication of the copper nanomaterial

### 5.2.3. Experimental Procedure for the *N*-arylation of imidazoles and benzimidazoles with arylboronic acids

In a thoroughly cleaned and dried 25 mL round bottom flask, 1 equiv (0.5 mmol) of the imidazole, 1.2 equiv (0.6 mmol) of the arylboronic acid and 10 wt% of the catalyst in 4 mL of the solvent (MeOH) were taken. The reaction mixture was allowed to stir at  $60\text{ }^\circ\text{C}$  for the required time. After completion (as indicated by TLC), the reaction mixture was filtered through a plug of celite and was subjected to extraction with the

ethyl acetate–water system (3 X 15 mL). The combined organic phases were then dried with sodium sulfate and concentrated in vacuum to obtain the crude product. The crude product was then purified using column chromatography (using ethyl acetate – hexanes) to afford the pure *N*-arylated product (**Scheme 5.2**).



**Scheme 5.2.** General procedure for the *N*-arylation of imidazoles with arylboronic acids

### 5.3. Results and discussion

#### 5.3.1. Characterisation of the Cu-nanomaterial

##### 5.3.1.1. FTIR Analysis

The Fourier-transform infrared (FTIR) spectra of copper acetate, Cu(OAc)<sub>2</sub>, and the copper nanomaterial were recorded and are presented in **Figure 5.1**. The analysis of these spectra reveals significant differences in the vibrational modes, especially in the range of 1000-500 cm<sup>-1</sup>, where metal-ligand interactions are typically observed. In the case of copper acetate, distinct peaks appear in this region, corresponding to the characteristic vibrations associated with Cu(II) species bonded to acetate ligands. However, for the nanomaterial, the diminished vibrational modes in this region suggest a notable absence of metal-ligand interactions.

This loss indicates a decomposition or alteration of the Cu(II) species upon heat treatment at 190 °C, likely due to thermal breakdown or removal of the acetate ligands. The reduction in these specific vibrational signals implies that the nanomaterial primarily consists of decomposed copper species, possibly transforming into Cu(I) or Cu(0) forms [22].

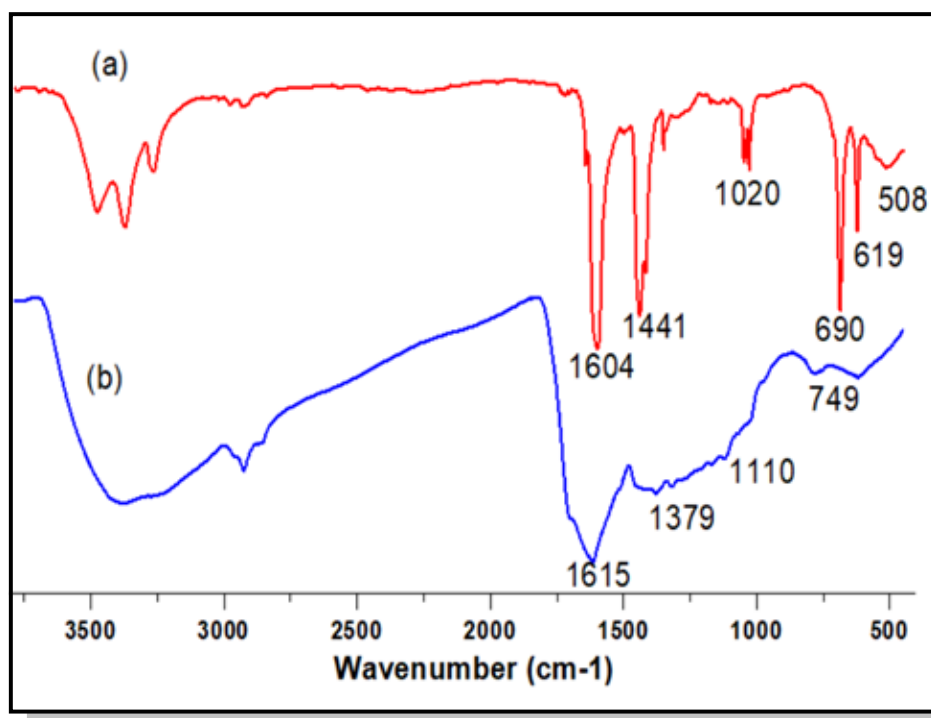


**Figure 5.1.** FTIR Spectra of (a) Copper (II) acetate; (b) Copper nanomaterial obtained using waste papaya peel extract

#### 5.3.1.2. Electron microscopic and energy dispersive spectroscopic analyses

SEM imaging reveals that the nanoparticles exhibit a uniform spherical morphology, which is often desirable for various applications due to its potential to enhance surface area and reactivity. The spherical shape observed here indicates a controlled synthesis process, which is crucial for achieving consistency in nanomaterial performance across applications. Additionally, the SEM image highlights the porous nature of the material. The pores provide channels for easy access to the surface area within the nanoparticles, which can increase catalytic activity (**Figure 5.2**).

The energy dispersive spectroscopy (EDS) mapping and energy dispersive X-ray (EDX) data of the synthesised nanomaterial are presented in **Figure (a, b, c, and d)**. The EDS mapping images highlight a uniform distribution of copper and oxygen across the material, indicating consistent dispersion of these elements throughout the sample. Additionally, the EDX data provides quantitative insight into the elemental composition of the material, showing that it comprises approximately 61% carbon, 20.81% oxygen, and 17.52% copper, as displayed in **Figure 5.3(e)**. This composition

suggests that carbon is the primary component, likely forming the matrix or scaffold of the material

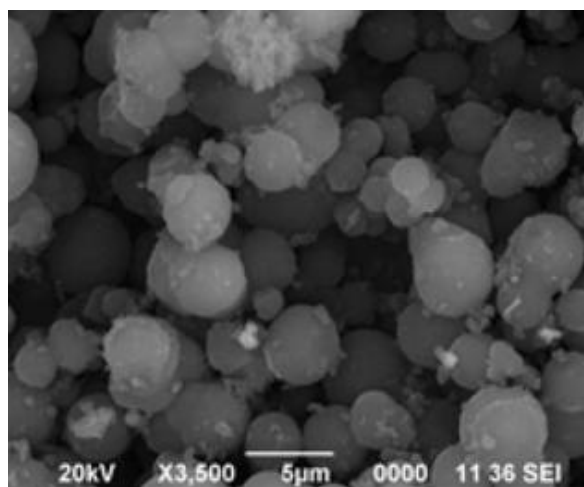


**Figure 5.2.** SEM image of the Cu-nanomaterial showing spherical morphology

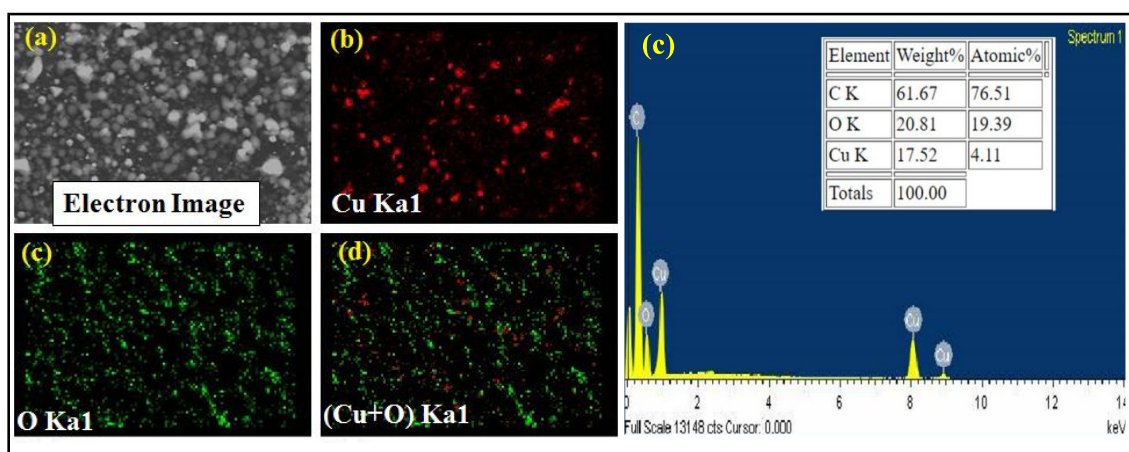


**Figure 5.3.** (a)–(d) SEM-EDS mappings of the nanocatalyst; (e) EDX spectrum of the nanocatalyst

#### 5.3.1.3. Solid UV Spectroscopic analysis.

**Figure 5.4** depicts the solid UV spectrum of the nanomaterial in comparison with copper acetate precursor. The vanishing of the peak at 489 nm in the catalytic material shows the reduction of Copper (II).



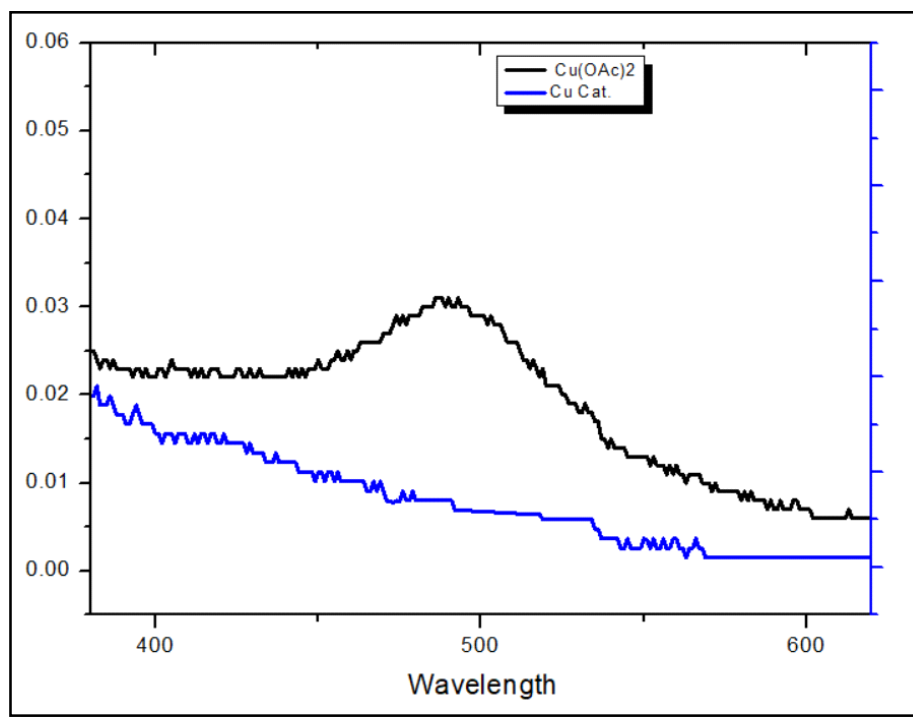


**Figure 5.4.** Solid UV-Vis spectrum of the nanocatalyst

#### 5.3.1.4. Transmission electron microscopy (TEM) analysis

The Transmission Electron Microscopy (TEM) images of the nanocatalyst reveal the formation of well-dispersed nanoparticles on a carbon-rich support derived from waste papaya peels. This sustainable carboniferous support not only provides an environmentally friendly substrate but also enhances the distribution and stability of the catalytic nanoparticles. High-resolution TEM (HR-TEM) images offer further insight into the nanostructure, showing the presence of both metallic copper (0) and copper (I) species. These are clearly distinguished by the diffraction fringes observed in the images, with measured  $d$ -spacings of 0.2 and 0.25 nm for the (111) planes of Cu(0), Cu(I) respectively (**Figure 5.5** (a)–(c)). The presence of these two oxidation states is significant, as it suggests that the catalyst may exhibit bifunctional properties, potentially enhancing its catalytic activity for redox reactions by providing sites that can facilitate electron transfer. The nanoparticles exhibit an average particle size of 6.6 nm as evident from the particle size distribution histogram (**Figure 5.5** (d)).

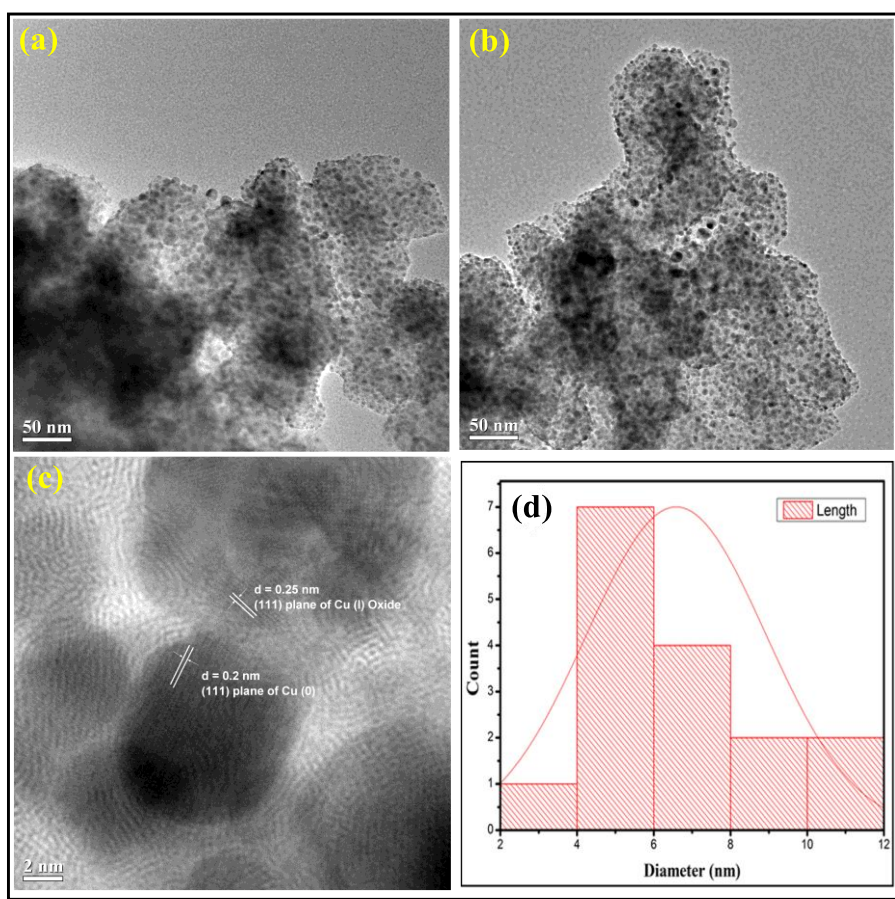


**Figure 5.5.** (a) – (c) TEM and HR-TEM images of the nanocatalyst; (d) Particle size distribution histogram for the nanocatalyst

#### 5.3.1.5. Powder X-Ray diffraction (PXRD) analysis

We conducted powder X-ray diffraction (XRD) analysis for copper nanoparticles synthesised at 463 K (Cu-463K), as shown in **Figure 5.6**, to investigate their crystalline nature. The XRD pattern reveals a significant feature: a weak signal at a diffraction angle of  $36.4^\circ$ , which corresponds to (111) plane present in cubic  $\text{Cu}_2\text{O}$  structure, as identified by the Joint Committee on Powder Diffraction Standards (JCPDS) file 78-2076. This indicates the formation of  $\text{Cu}_2\text{O}$  due to a partial *in-situ* transformation of Cu to  $\text{Cu}_2\text{O}$  at elevated temperatures. The emergence of  $\text{Cu}_2\text{O}$  can be attributed to the reaction of copper with steam under high-temperature conditions. While pure copper is typically not seen to undergo reaction with liquid water, it interacts with steam to produce gaseous hydrogen and corresponding oxides. At  $190^\circ\text{C}$ , water is predominantly in its vapor phase, which increases the likelihood of copper oxidation. This leads to the transformation of some Cu(0) species

into  $\text{Cu}_2\text{O}$ . Thus, the observed diffraction peaks confirm that high temperatures and increased water vapor pressure play a crucial role in the oxidation process, resulting in the formation of  $\text{Cu}_2\text{O}$  nanostructures.

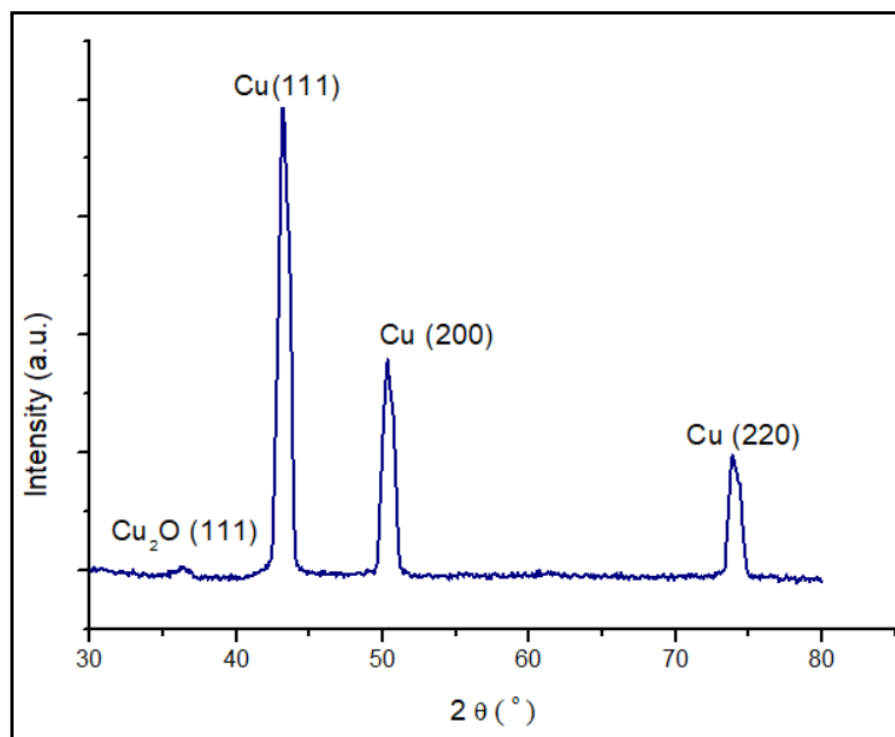


**Figure 5.6.** Powder XRD pattern for the synthesised nanomaterial

#### 5.3.1.6. X-Ray Photoelectron Spectroscopy (XPS) analysis

Further confirmation of the composition and oxidation states of copper nanoparticles (Cu NPs) in the made nanocatalyst was provided by X-ray photoelectron spectroscopy (XPS). As shown in **Figure 5.7**, the in the high-resolution deconvoluted Cu 2p XPS spectrum of the material s key peaks at 932.63 eV and 952.4 eV, correspondence to Cu 2p<sub>3/2</sub> and Cu 2p<sub>1/2</sub> were observed, respectively which indicate the occurrence of Cu(0) and Cu(I) together. The emergence of faint satellite peaks at 943.3 eV and 962.1 eV confirm the existence of Cu(I) species, corroborating the earlier observation of a  $\text{Cu}_2\text{O}$  diffraction peak in the XRD analysis (**Figure 5.6 (a)**). The C 1s spectrum of the material (**Figure 5.7 (b)**) shows peaks at 284.7 eV, 287.4 eV respectively, which are due to the presence of carbon – oxygen bonds, present in the papaya peel extract used during synthesis. Additionally, the O 1s XPS spectrum of the material (**Figure 5.7 (c)**) reveals a distinct signal at 530.9 eV, which is attributed to the copper oxygen bond of  $\text{Cu}_2\text{O}$ . These XPS findings confirm the formation of both metallic copper (Cu) and

Cu<sub>2</sub>O.. The contribution of the papaya peel extract to the stabilisation of the nanoparticles is also evident, as indicated by the carbon-related binding energy peaks observed in the C 1s spectrum. This comprehensive characterisation reinforces the conclusion that the synthesis conditions promote partial oxidation of Cu(0) to Cu<sub>2</sub>O aligning with the structural observations from XRD.

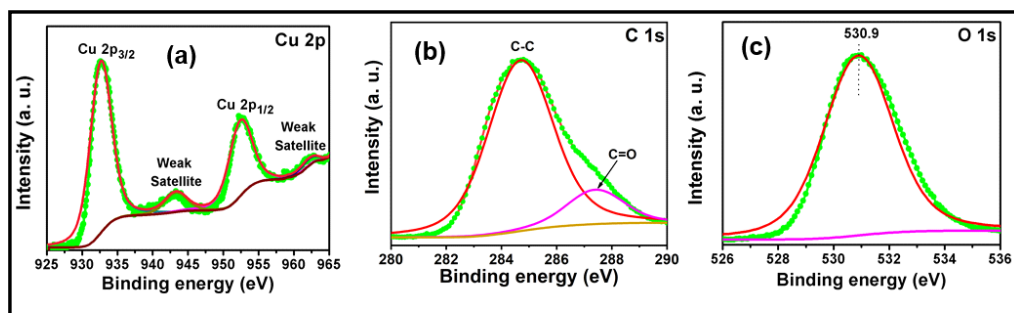


**Figure 5.7.** (a) Cu 2p spectrum, (b) C 1s spectrum, (c) O 1s spectrum of the nanocatalyst

#### 5.3.1.7. Thermogravimetric Analysis (TGA)

The thermogravimetric analysis (TGA) profile of the nanomaterial is presented below in **Figure 5.8**. The initial weight loss, observed between approximately 80 °C and 150 °C, corresponds to the evaporation of volatile components and water. This accounts for a reduction in mass of about 0.23 mg, indicating the removal of physically adsorbed moisture and other low-boiling-point substances. A more significant weight loss, amounting to approximately 0.32 mg, is recorded from 380 °C to 420 °C. This is attributed to the thermal degradation of carbonaceous or carboniferous material present in the nanomaterial, likely resulting from the breakdown of organic residues or carbon-containing compounds. This stage signifies the thermal stability of the material under elevated temperatures.

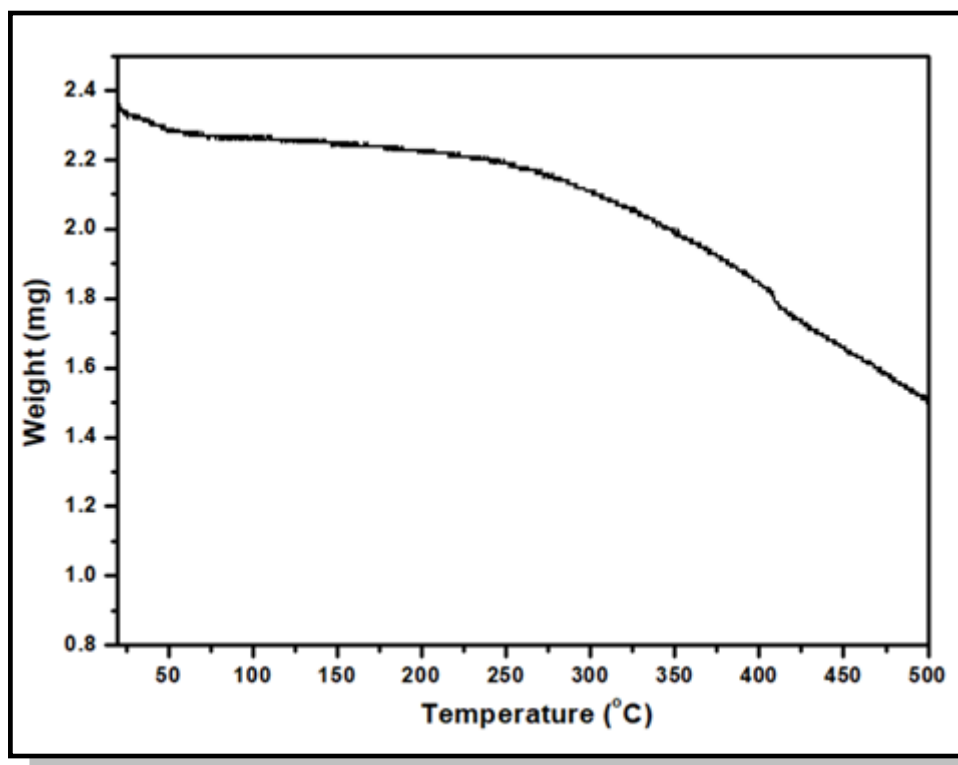


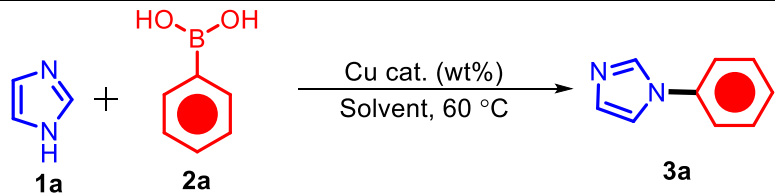
**Figure 5.8.** TGA profile of the material

### 5.3.2. Optimisation of the reaction conditions

The catalytic efficiency of the synthesised Cu nanomaterial catalyst was carefully evaluated for the C-N cross-coupling reaction between arylboronic acids and imidazoles. To determine the optimal reaction conditions, phenylboronic acid (**1a**) and imidazole (**2a**) were selected as model substrates. The reactions were conducted in methanol ( $\text{CH}_3\text{OH}$ ) at 60 °C, focusing on optimising catalyst loading, substrate ratios, and solvent effects, as summarised in **Table 5.1**. When 10 wt% of the catalyst was employed with 1 equivalent of **1a** and 1.2 equivalents of **2a**, the product **3a** was obtained in a 55% yield after 10 hours at 60 °C (**Table 5.1, Entry 1**). This relatively low yield and longer reaction time indicated that the catalyst loading was insufficient for efficient conversion of the starting materials. Increasing the catalyst amount to 15 wt% significantly enhanced the reaction efficiency, improving the yield to 85% and reducing the reaction time to 7 hours under the same conditions (**Table 5.1, Entry 2**). A further increase in catalyst loading to 20 wt% led to an even higher yield of 90%, showcasing that the availability of more active sites facilitated better catalytic activity (**Table 5.1, Entry 3**). However, increasing the boronic acid equivalent to 1.5 did not result in any significant advantage. Instead, the yield dropped slightly to 87% (**Table**

**5.1, Entry 4**). This decrease may be ascribed to possible parallel processes or unproductive consumption of the excess boronic acid. Similarly, using 1 equivalent of boronic acid instead of 1.2 equivalents resulted in a lower yield of 83% (**Table 5.1, Entry 5**), indicating that a precise balance in the substrate ratio is crucial for optimal coupling efficiency. The effect of the reaction medium on the product yield was also examined. When water was used as the solvent, the yield dropped to 60% (**Table 5.1, Entry 6**), likely due to limited solubility of the reactants and catalyst in an aqueous medium. Replacing methanol with 2-methyltetrahydrofuran led to no detectable product formation after 10 hours (**Table 5.1, Entry 7**), indicating that this solvent was unsuitable for the reaction. Using a 1:1 mixture of water and methanol provided a moderate yield of 55% in 7 hours (**Table 5.1, Entry 8**), suggesting that methanol alone is more effective in promoting the reaction. Furthermore, the reaction in DMF resulted in a poor yield of only 30% (**Table 5.1, Entry 9**), likely due to unfavorable interactions between the catalyst and solvent, or reduced reactivity of the substrates in this medium. The temperature dependence of the reaction was also evaluated, revealing that conducting the reaction at room temperature caused no product formation. This lack of activity at lower temperatures underscores the necessity of elevated temperatures to activate the catalyst and drive the coupling reaction effectively. These results demonstrate the critical role of optimising reaction parameters, including catalyst loading, substrate ratio, solvent, and temperature, in achieving high efficiency for the C-N cross-coupling reaction. The use of 20 wt% of the catalyst, 1.2 equivalents of boronic acid, methanol as the solvent, and at 60 °C were identified as the ideal conditions to maximise the yield of the desired product.

**Table 5.1.** Optimisation of the reaction conditions

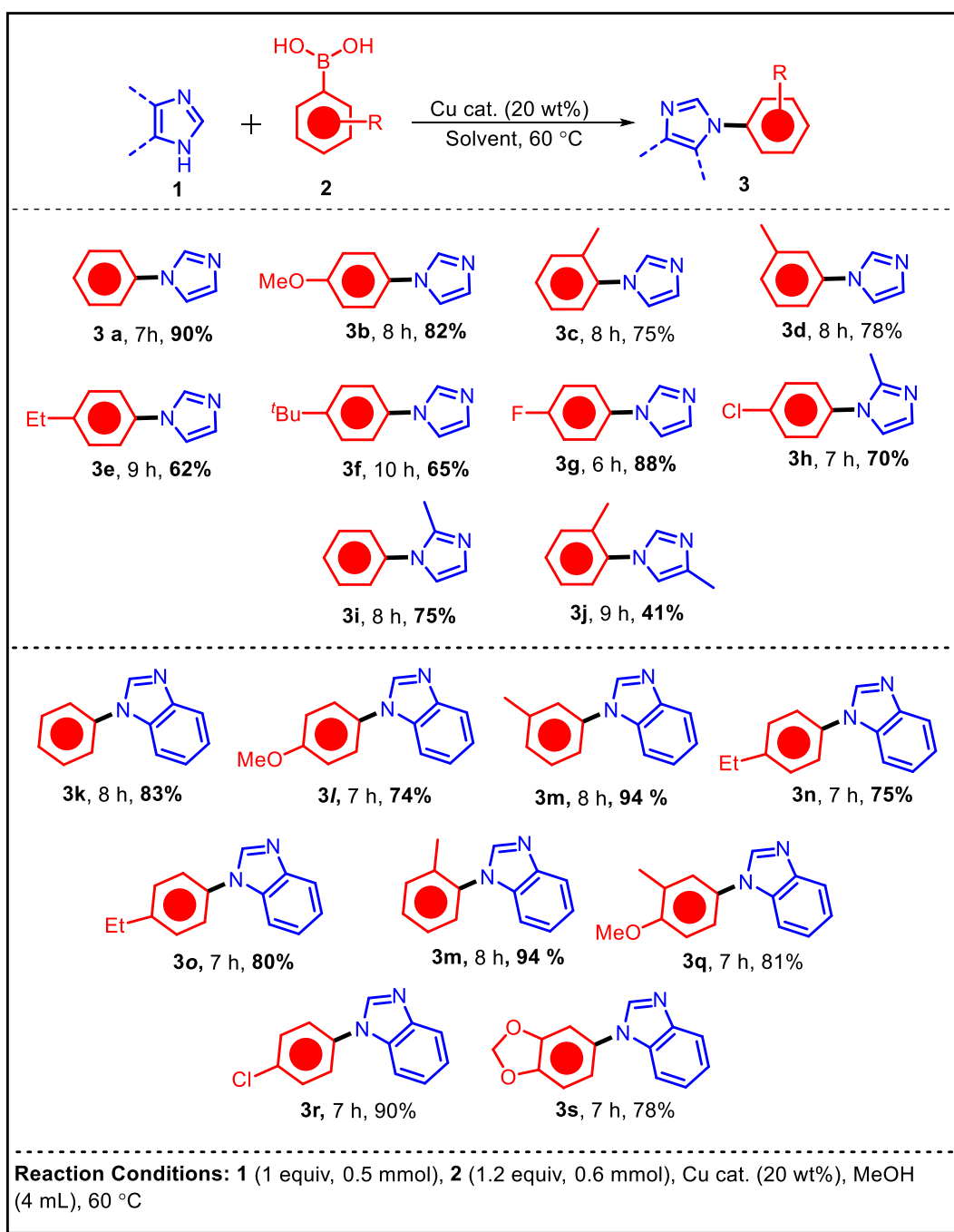
				
Sl. No.	Catalyst (wt%)	Solvent (mL)	Time (h)	Yield (%) <sup>[a]</sup>
1	10	MeOH (4 mL)	10	55
2	15	MeOH (4 mL)	7	85
3	20	MeOH (4 mL)	7	90
4	20	MeOH (4 mL)	7	87 <sup>[b]</sup>
5	20	MeOH (4 mL)	9	83 <sup>[c]</sup>
6	20	H <sub>2</sub> O (4 mL)	8	60
7	20	2-MeTHF (4 mL)	10	n.r.
8	20	H <sub>2</sub> O : MeOH (1:1) (4 mL)	7	55
9	20	DMF (4 mL)	10	30
10	20	MeOH (4 mL)	10	n.r. <sup>[d]</sup>
<b>Reaction conditions:</b> Imidazole (1 equiv, 0.5 mmol), Phenyl boronic acid (1.2 equiv, 0.6 mmol), Solvent (4 ml), 60 °C, <sup>[a]</sup> Isolated yield, <sup>[b]</sup> <b>1a</b> (1 equiv), <b>2a</b> (1.5 equiv), <sup>[c]</sup> <b>1a</b> (1 equiv), <b>2a</b> (1 equiv), <sup>[d]</sup> Reaction done at r.t.				

### 5.3.3. Substrate scope studies

With the refined reaction parameters established, the extent of the reaction was examined using a variety of electronically varied substrates. The results of these studies are summarised in **Table 5.2**. The coupling of phenylboronic acid with imidazole yielded 90% of the product **3a** in 7 hours, highlighting the effectiveness of the catalytic system. When 4-methoxyphenylboronic acid was coupled with imidazole, the reaction produced 82% of the product **3b** in 8 hours. The usage of sterically caught up substrates, such as 2- methyl and 3-methylphenylboronic acid, resulted in products **3c** and **3d** with yields of 75% and 78%, respectively. Additionally, reaction of 4-ethylphenylboronic acid with imidazole afforded 62% of the product **3e** in 9 hours. Using 4-tertiarybutylphenylboronic acid, 65% of the product **3f** was obtained in 10 hours. Interestingly, the coupling efficiency improved with 4-

fluorophenylboronic acid, yielding 88% of product **3g**, possibly due to the electron-withdrawing nature of the fluorine atom enhancing reactivity. For substrates with 2-methylimidazole, the coupling of 4-chlorophenylboronic acid yielded 70% of product **3h** in 7 hours, while the coupling with phenylboronic acid resulted in a yield of 75% for product **3i** in 8 hours. In succession, 4-methylimidazole coupled with 2-methylphenylboronic acid to give 41% of the product **3j** in 9 hours. The space of the catalytic system was further stretched to benzimidazoles. The *N*-arylation of benzimidazole with phenylboronic acid delivered 83% of the product **3k**, demonstrating the broad applicability of the system. Substituted arylboronic acids, such as 4-methoxyphenylboronic acid, gave 74% of product **3l** in 7 hours. Furthermore, using 3-methyl- and 4-ethylphenylboronic acids afforded products **3m** and **3n** with yields of 94% and 75% in 8 and 7 hours, respectively. The coupling of 4-nitrophenylboronic acid with benzimidazole yielded 80% of product **3o** in 7 hours, while 2-methylphenylboronic acid delivered 89% of product **3p**. When 3-methyl-4-methoxyphenylboronic acid was utilised, 81% of product **3q** was obtained. Similarly, the coupling of 4-chlorophenylboronic acid with benzimidazole resulted in an impressive 90% yield of the product **3r** in 7 hours. Lastly, the reaction of 3,4-methylenedioxyphenylboronic acid with benzimidazole gave 81% of product **3s**. These results showcase the versatility and efficiency of the system across a wide variety of electronically and sterically diverse substrates, making it a robust platform for *N*-arylation reactions of imidazoles.



**Table 5.2.** Substrate scope studies for C-N bond formation

### 5.3.4. Catalyst reusability studies

The catalyst's reusability was examined for the cross-coupling reaction under the established reaction protocol. Our findings indicate that the catalyst retains its activity effectively for three cycles of use, while a gradual decline in catalytic performance was observed in both reactions, as shown in **Figure 5.9**. This reduction in activity could be attributed to surface morphology changes or processes such as

Ostwald's thermodynamic ripening, which may cause nanoparticle aggregation and cluster development under the effect of the solvent or over time.

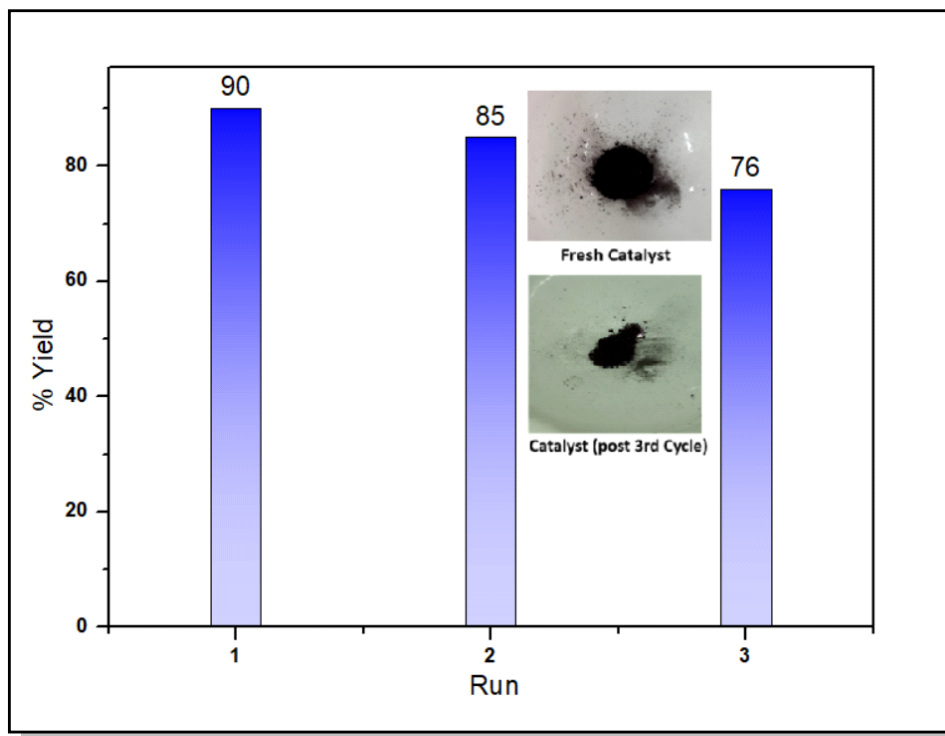


**Figure 5.9.** Catalyst reusability profile

### 5.3.5. Catalyst analysis post reuse

#### 5.3.5.1 SEM and TEM analysis

Scanning electron microscopy (SEM) was used to analyse the retrieved catalyst to study its morphological changes after use. The SEM images revealed that the catalyst particles had agglomerated, forming clusters with irregular shapes. This structural transformation likely contributes to the observed decrease in catalytic efficiency over successive reaction cycles (**Figure 5.10**).

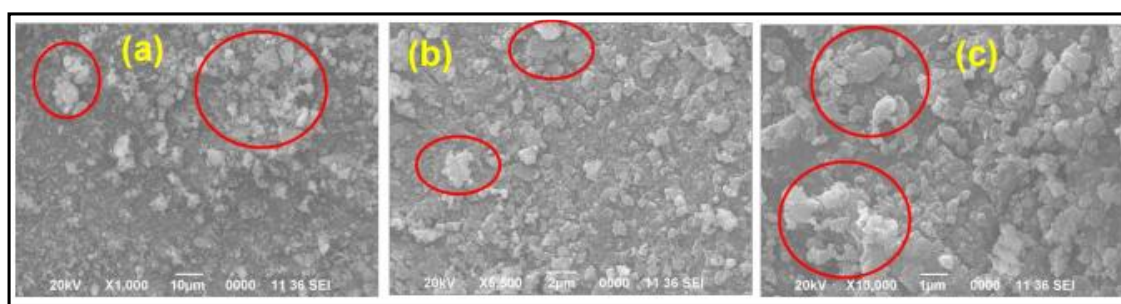


**Figure 5.10.** SEM images of the catalyst post 3<sup>rd</sup> catalytic cycle

TEM image of the catalyst post reuse also highlights the agglomeration of the catalyst post reuse (**Figure 5.11**).

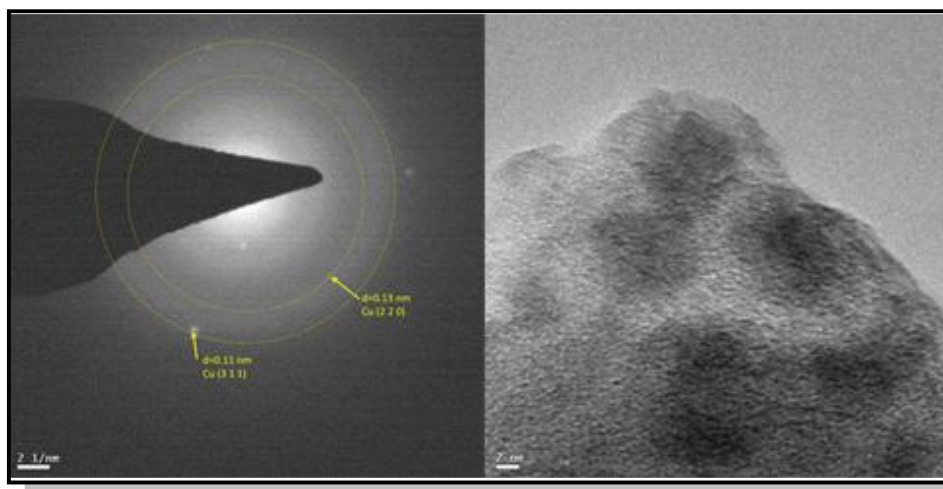


**Figure 5.11.** TEM image post reuse showing agglomeration

#### 5.3.5.2. Powder XRD analysis

Three distinct sharp peaks at  $43.17^\circ$ ,  $50.26^\circ$ , and  $73.93^\circ$  were revealed in the PXRD analysis of the reused catalyst sample after the third catalytic cycle, corresponding to the crystal planes (1 1 1), (2 0 0), and (2 2 0) of *fcc* lattice of Cu, as identified by comparison with the JCPDS file no. 85-1326. Additionally, a minor peak was observed at  $36.39^\circ$ , which was attributed to the (1 1 1) plane of cubic  $\text{Cu}_2\text{O}$  nanostructures, based on the JCPDS file no. 78-2076. This suggests that while the primary structure of the catalyst remains predominantly metallic Cu, some oxidation to  $\text{Cu}_2\text{O}$  may have occurred during the catalytic cycles, possibly contributing to the observed changes in catalytic performance (**Figure 5.12**).

#### 5.3.5.3. XPS analysis

Two distinct peaks at 934.13 eV and 953.72 eV, corresponding to Cu 2p<sub>3/2</sub> and Cu 2p<sub>1/2</sub>, respectively, are displayed in the high-resolution deconvoluted Cu 2p XPS spectrum of the reused catalyst. These peaks are indicative of Cu(II) nanoparticles (NPs) in the Cu-463K sample. This assignment is further supported by the presence of characteristic shake-up satellite peaks at 943.52 eV and 962.87 eV (**Figure 5.13 (a)**), which are commonly associated with the Cu(II) oxidation state. The separation energy peaks at 284.63 eV, 285.88 eV, and 287.09 eV are displayed in the

high-resolution C 1s XPS spectrum of the nanocatalyst, as shown in **Figure 5.13 (b)**. These peaks are ascribed to the carbon-oxygen bonds in functional groups. These peaks are attributed to the C–O, C=O, and O–C=O functional groups, respectively. The presence of these groups indicates surface modifications or interactions of the catalyst with the reaction medium during the catalytic cycles, potentially contributing to changes in its chemical environment and performance.

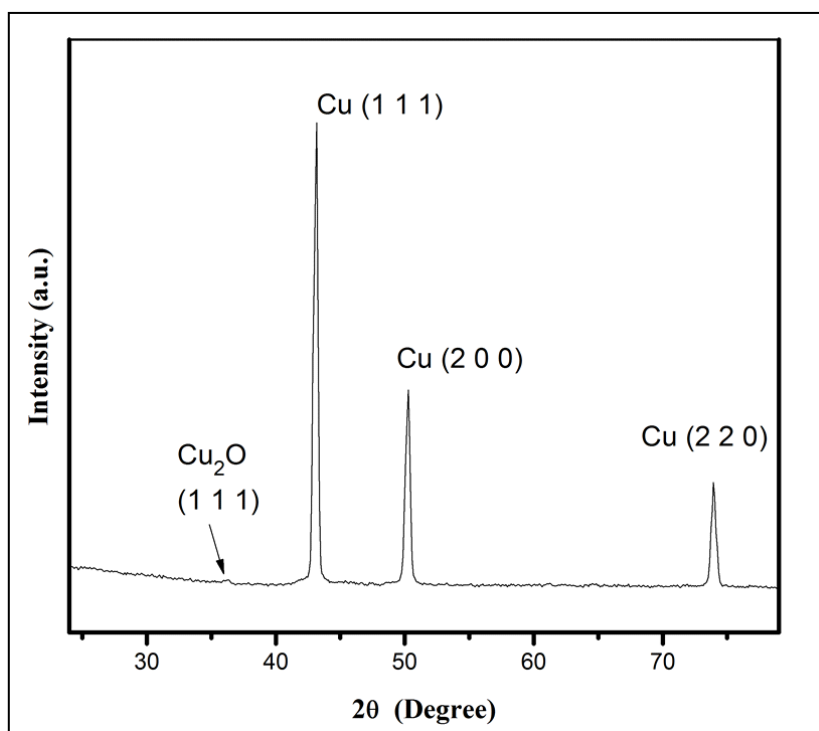


**Figure 5.12.** PXRD pattern post 3<sup>rd</sup> cycle

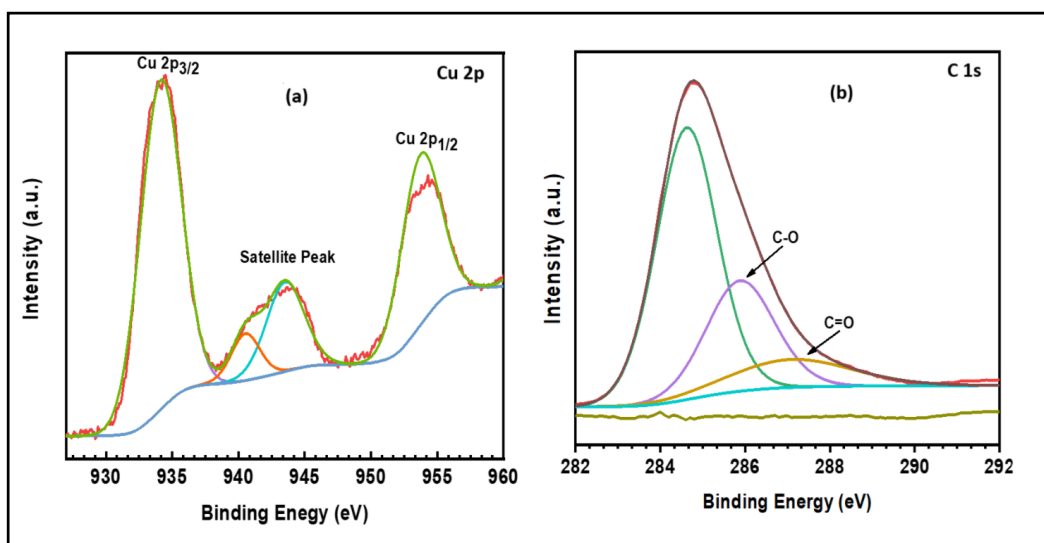
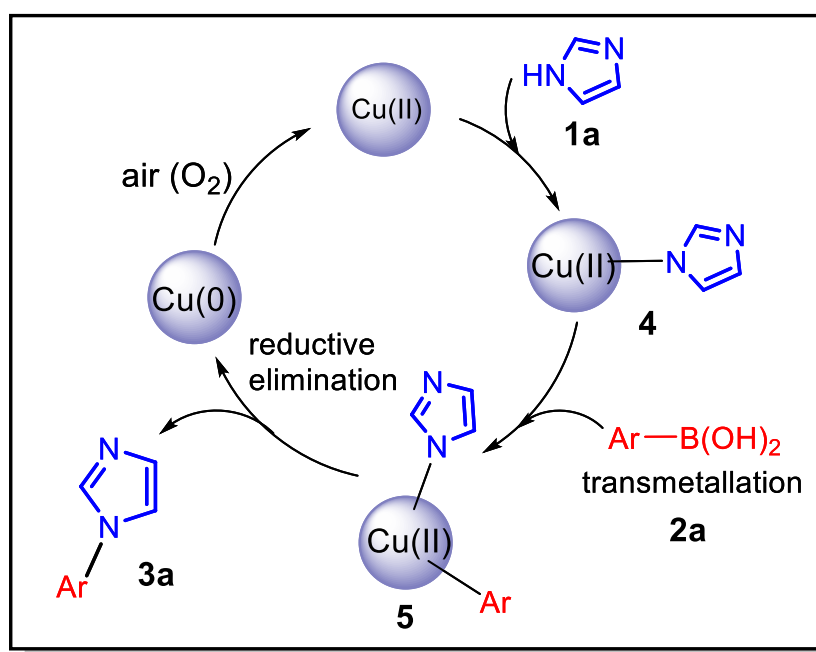


**Figure 5.13.** a) Cu 2p and b) C 1s spectra of the reused catalyst

### 5.3.6. Reaction Mechanism

The process begins with the oxidation of copper (0) in the nanomaterial to copper (II), which enables the coordination of imidazole to the copper center. This coordination step is followed by a transmetallation reaction, where the imidazole ligand is transferred to the copper center, forming the aryl-imidazolyl copper (II) species (5). After this, a reductive elimination step occurs, in which the aryl group is removed from the copper center, leading to the regeneration of copper (0). This cycle of oxidation, coordination, transmetallation, and reductive elimination is key to the catalytic activity of the copper nanomaterial in various coupling reactions (**Scheme 5.3**).

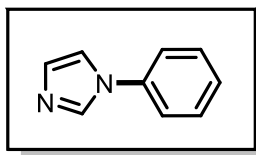


**Scheme 5.3.** Reaction mechanism for *N*-arylation

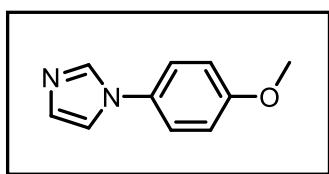
### 5.4. Conclusion

This methodology presents a cost-effective and sustainable approach for synthesising copper nanoparticles (NPs) by utilising farm-waste materials. The direct fabrication of copper (I) oxide NPs on the copper surface, induced by gas-phase H<sub>2</sub>O/O<sub>2</sub> stimuli without relying on orthodox reductants, presents an environmentally welcoming approach to metal nanoparticle synthesis. Additionally, the hybrid Cu<sub>2</sub>O/Cu NPs enable the synthesis of a diverse range of *N*-arylated imidazole and benzimidazole derivatives. The catalytic performance is attributed to the interaction between the

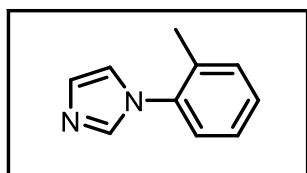
Cu(0) and Cu(I) surfaces, which show noteworthy action in coupling reactions involving arylboronic acids that form carbon-carbon and carbon-nitrogen linkages. Notably, the catalyst showcases excellent reusability for C–N coupling reactions, maintaining its activity over multiple cycles with minimal loss in efficiency.

5.5.  $^1\text{H}$  and  $^{13}\text{C}$  NMR Data

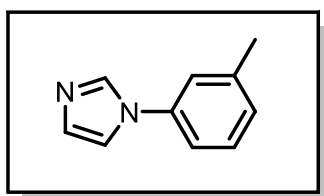
**1. 3a. 1-Phenyl-1H-imidazole**, pale yellow oil:  $^1\text{H}$  NMR (400 MHz, DMSO- $\text{D}_6$ )  $\delta$  8.22 (s, 1H), 7.70 (s, 1H), 7.62 – 7.56 (m, 2H), 7.51 – 7.39 (m, 2H), 7.38 – 7.23 (m, 1H), 7.08 (s, 1H).  $^{13}\text{C}$  NMR (100 MHz, DMSO- $\text{D}_6$ )  $\delta$  137.5, 136.1, 130.5, 130.4, 127.4, 120.9, 118.5.



**2. 3b. 1-(4-Methoxyphenyl)-1H-imidazole**, pale yellow oil:  $^1\text{H}$  NMR (400 MHz, DMSO- $\text{D}_6$ )  $\delta$  (ppm) 7.72 (s, 1), 7.26 (d,  $J$  = 7.8 Hz, 2H), 7.16 – 7.14 (m, 2H), 6.91 (d,  $J$  = 7.8 Hz, 2H) 3.8 (s, 3H).  $^{13}\text{C}$  NMR (100 MHz, DMSO- $\text{D}_6$ )  $\delta$  159.0, 135.9, 130.8, 130.2, 123.2, 119.0, 115.0, 55.6.

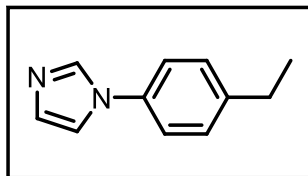


**3. 3c. 1-(2-Methylphenyl)-1H-imidazole**, pale yellow oil:  $^1\text{H}$  NMR (400 MHz, DMSO- $\text{D}_6$ )  $\delta$  (ppm) 7.58 (s, 1H), 7.33 – 7.18 (m, 5H), 7.03 (s, 1H), 2.15 (s, 3H).  $^{13}\text{C}$  NMR (100 MHz, DMSO- $\text{D}_6$ )  $\delta$  (ppm) 138.2, 137.2, 133.7, 131.7, 129.2, 129.0, 127.5, 126.9, 121.4, 18.1.

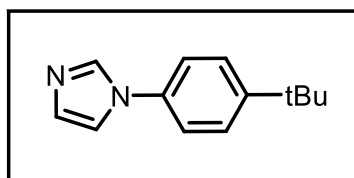


**4. 3d. 1-(m-Tolyl)-1H-imidazole**, pale yellow oil:  $^1\text{H}$  NMR (400 MHz, CHLOROFORM- $\text{D}$ )  $\delta$  (ppm) 8.27 - 8.15 (m, 1H), 7.67 (s, 1H), 7.47 – 7.28 (m, 3H), 7.24 – 7.05 (m, 2H),

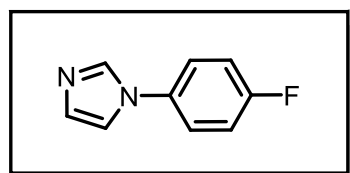
2.32 (s, 3H).  $^{13}\text{C}$  NMR (100 MHz, CHLOROFORM-D)  $\delta$  (ppm) 140.1, 137.4, 136.0, 130.4, 130.1, 128.0, 121.4, 118.5, 117.9, 21.5.



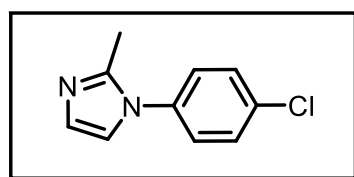
**5. 3e. 1-(4-Ethylphenyl)-1H-imidazole**, colourless oil:  $^1\text{H}$  NMR (400 MHz, CHLOROFORM-D)  $\delta$  (ppm) 7.81 (s, 1H), 7.28 – 7.23 (m, 5H), 7.17 (s, 1H), 2.71 – 2.65 (q,  $J$  = 6.6 Hz, 2H) 1.27 – 1.23 (t,  $J$  = 6.6 Hz, 3H).  $^{13}\text{C}$  NMR (100 MHz, CHLOROFORM-D)  $\delta$  (ppm) 144.0, 138.7, 135.3, 130.2, 129.3, 121.7, 118.6, 28.4, 15.6.



**6. 3f. 1-(4-(Tert-butyl)phenyl)-1H-imidazole**, colourless oil:  $^1\text{H}$  NMR (400 MHz, CHLOROFORM-D)  $\delta$  (ppm) 7.78 (s, 1H), 7.3 (m, 2H), 7.25 (m, 2H), 7.20 (s, 1H), 7.15 (s, 1H), 1.30 (s, 9H).  $^{13}\text{C}$  NMR (400 MHz, CHLOROFORM-D)  $\delta$  (ppm) 150.6, 135.6, 134.8, 130.2, 126.7, 121.1, 118.3, 34.6, 31.3.

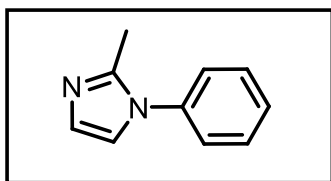


**7. 3g. 1-(4-Fluorophenyl)-1H-imidazole**, yellow oil:  $^1\text{H}$  NMR (400 MHz, CHLOROFORM-D)  $\delta$  (ppm) 7.76 (s, 1H), 7.34 – 7.31 (m, 2H), 7.18 – 7.12 (m, 4H).  $^{13}\text{C}$  NMR (400 MHz, CHLOROFORM-D)  $\delta$  (ppm) 162.9, 160.5, 135.8, 133.6, 130.4, 123.5, 119.0, 116.9.

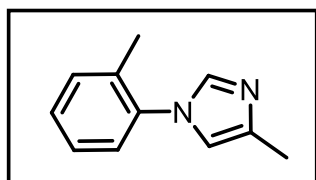




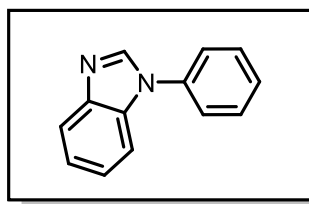
**8. 3h. 1-(4-Chlorophenyl)-2-methyl-1H-imidazole**, yellow oil:  $^1\text{H}$  NMR (400 MHz, DMSO- $\text{D}_6$ )  $\delta$  (ppm) 7.55 – 7.53 (d,  $J$  = 8 Hz, 2H), 7.45 – 7.43 (d,  $J$  = 8 Hz, 2H), 7.39 (s, 1H), 6.89 (s, 1H), 2.24 (s, 3H).  $^{13}\text{C}$  NMR (100 MHz, DMSO- $\text{D}_6$ )  $\delta$  (ppm) 137.0, 134.6, 132.9, 130.0, 127.9, 127.5, 127.4, 14.1.



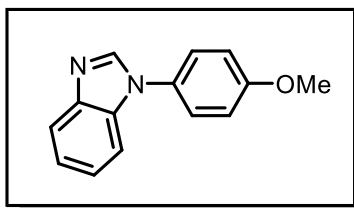
**9. 3i. 2-Methyl-1-phenyl-1H-imidazole**, light yellow oil:  $^1\text{H}$  NMR (400 MHz, DMSO- $\text{D}_6$ )  $\delta$  (ppm) 7.52 – 7.43 (m, 2H), 7.41 – 7.38 (m, 3H), 7.23 (s, 1H), 6.88 (s, 1H), 2.24 (s, 3H).  $^{13}\text{C}$  NMR (100 MHz, DMSO- $\text{D}_6$ )  $\delta$  (ppm) 138.1, 130.1, 128.4, 127.7, 125.7, 121.4, 121.2, 14.1.



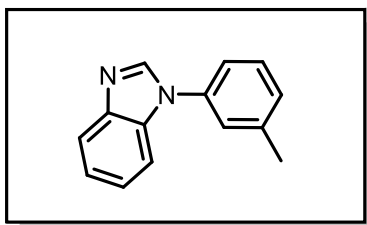
**10. 3j. 4-Methyl-1-(o-tolyl)-1H-imidazole**, yellow oil:  $^1\text{H}$  NMR (400 MHz, DMSO- $\text{D}_6$ )  $\delta$  (ppm) 7.80 – 7.77 (m, 2H), 7.59 (s, 1H), 7.37 – 7.26 (m, 3H), 2.40 – 2.37 (m, 3H), 2.31 – 2.27 (m, 3H).  $^{13}\text{C}$  NMR (100 MHz, DMSO- $\text{D}_6$ )  $\delta$  (ppm) 137.6, 137.4, 137.2, 133.5, 131.7, 128.8, 127.4, 126.7, 117.6, 18.5, 14.1.



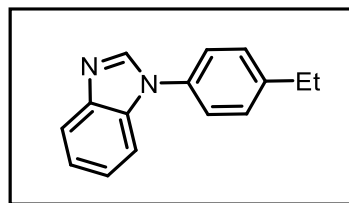
**11. 3k. 1-Phenyl-1H-benzo[d]imidazole**, pale yellow solid:  $^1\text{H}$  NMR (400 MHz, DMSO- $\text{D}_6$ )  $\delta$  (ppm) 8.52 (s, 1H), 7.82 – 7.73 (m, 1H), 7.64 – 7.48 (m, 5H), 7.41 (m, 1H), 7.31 – 7.21 (m, 2H).  $^{13}\text{C}$  NMR (100 MHz, DMSO- $\text{D}_6$ )  $\delta$  (ppm) 144.4, 143.7, 136.5, 133.6, 130.6, 128.2, 124.1, 124.0, 123.0, 120.5, 111.1.



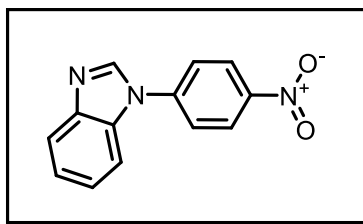
**12. 3l. 1-(4-Methoxyphenyl)-1H-benzo[d]imidazole**, pale yellow solid:  $^1\text{H}$  NMR (400 MHz, DMSO- $\text{D}_6$ )  $\delta$  (ppm) 8.42 (s, 1H), 7.79 – 7.67 (m, 1H), 7.52 (d,  $J = 9.0$  Hz, 2H), 7.48 – 7.43 (m, 1H), 7.25 (m, 2H), 7.11 (d,  $J = 9.0$  Hz, 2H), 3.79 (s, 3H).  $^{13}\text{C}$  NMR (100 MHz, DMSO- $\text{D}_6$ )  $\delta$  (ppm) 159.2, 144.1, 144.0, 134.1, 129.3, 125.9, 123.8, 122.7, 120.4, 115.6, 111.0, 56.0.



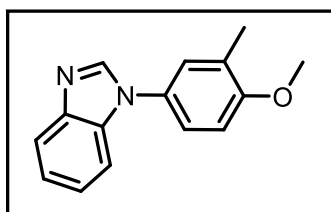
**13. 3m. 1-(3-Methylphenyl)-1H-benzo[d]imidazole**, pale yellow solid:  $^1\text{H}$  NMR (400 MHz, DMSO- $\text{D}_6$ )  $\delta$  (ppm) 8.49 (s, 1H), 7.81 – 7.68 (m, 1H), 7.60 – 7.50 (m, 1H), 7.48 – 7.35 (m, 3H), 7.31 – 7.19 (m, 3H), 2.37 (s, 3H).  $^{13}\text{C}$  NMR (100 MHz, DMSO- $\text{D}_6$ )  $\delta$  (ppm) 144.4, 143.8, 140.4, 136.4, 130.4, 130.3, 128.8, 124.7, 123.9, 122.9, 121.2, 120.5, 111.2, 21.4.



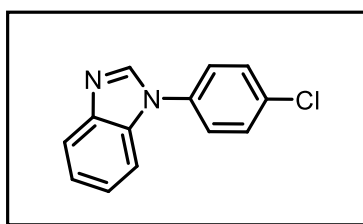
**14. 3n. 1-(4-Ethylphenyl)-1H-benzo[d]imidazole**, pale yellow solid:  $^1\text{H}$  NMR (400 MHz, CHLOROFORM- $\text{D}$ )  $\delta$  (ppm) 8.09 (s, 1H), 7.89 – 7.84 (m, 1H), 7.51 (m, 1H), 7.45 – 7.35 (m, 4H), 7.35 – 7.27 (m, 2H), 2.74 (q,  $J = 7.6$  Hz, 2H), 1.30 (t,  $J = 7.6$  Hz, 3H).  $^{13}\text{C}$  NMR (100 MHz, CHLOROFORM- $\text{D}$ )  $\delta$  (ppm) 144.5, 144.0, 142.5, 134.0, 133.9, 129.5, 124.2, 123.7, 122.8, 120.6, 110.6, 28.6, 15.6.



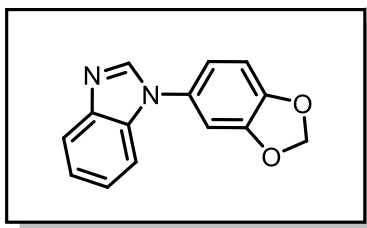
**15. 3o. 1-(4-Nitrophenyl)-1H-benzo[d]imidazole**, pale yellow solid:  $^1\text{H}$  NMR (400 MHz, CHLOROFORM-D)  $\delta$  (ppm) 8.41 (s, 1H), 8.31 (d,  $J$  = 8.2 Hz, 1H), 8.15 (s, 1H), 7.88 (d,  $J$  = 8.2 Hz, 2H), 7.80 – 7.76 (m, 1H), 7.54 (d,  $J$  = 9.3 Hz, 1H), 7.37 (d,  $J$  = 9.3 Hz, 2H).  $^{13}\text{C}$  NMR (100 MHz, CHLOROFORM-D)  $\delta$  (ppm) 149.3, 144.3, 141.8, 137.6, 133.2, 131.3, 129.4, 123.7, 122.6, 121.2, 118.8.



**16. 3q. 1-(4-Methoxy-3-methylphenyl)-1H-benzo[d]imidazole**, pale yellow solid:  $^1\text{H}$  NMR (400 MHz, CHLOROFORM-D)  $\delta$  (ppm) 8.03 (s, 1H), 7.85 (d,  $J$  = 9.2 Hz, 1H), 7.45 (d,  $J$  = 9.2 Hz, 1H), 7.36 – 7.19 (m, 4H), 6.96 – 6.94 (m, 1H), 3.90 (s, 3H), 2.29 (s, 3H).  $^{13}\text{C}$  NMR (100 MHz, CHLOROFORM-D)  $\delta$  (ppm) 157.6, 143.9, 142.7, 134.4, 128.7, 128.7, 126.9, 126.8, 123.5, 122.9, 122.6, 120.5, 110.5, 55.8, 16.5.



**17. 3r. 1-(4-Chloro-3-methylphenyl)-1H-benzo[d]imidazole**, yellow solid:  $^1\text{H}$  NMR (400 MHz, CHLOROFORM-D)  $\delta$  (ppm) 8.07 (s, 1H), 7.92 – 7.82 (m, 1H), 7.54 (d,  $J$  = 8.9 Hz, 2H), 7.48 (m, 1H), 7.45 (d,  $J$  = 8.9 Hz, 2H), 7.37 – 7.29 (m, 2H).  $^{13}\text{C}$  NMR (100 MHz, CHLOROFORM-D)  $\delta$  (ppm) 144.1, 142.1, 135.0, 134.0, 133.6, 130.4, 125.4, 124.0, 123.1, 120.9, 110.3.



**18. 3s. 1-(Benzo[d][1,3]dioxol-5-yl)-1H-benzo[d]imidazole**, yellow solid:  $^1\text{H}$  NMR (400 MHz, CHLOROFORM-D)  $\delta$  (ppm) 8.03 (s, 1H), 7.85 (d,  $J = 9.2$  Hz, 1H), 7.46 (d,  $J = 9.2$  Hz, 1H), 7.31 (m, 2H), 6.97 – 6.90 (m, 3H), 6.08 (s, 2H).  $^{13}\text{C}$  NMR (100 MHz, CHLOROFORM-D)  $\delta$  (ppm) 148.8, 147.6, 142.6, 130.3, 123.7, 122.8, 120.6, 118.0, 110.5, 109.0, 105.9, 105.2, 102.2, 100.0.

## 5.6. Representative NMR Spectra

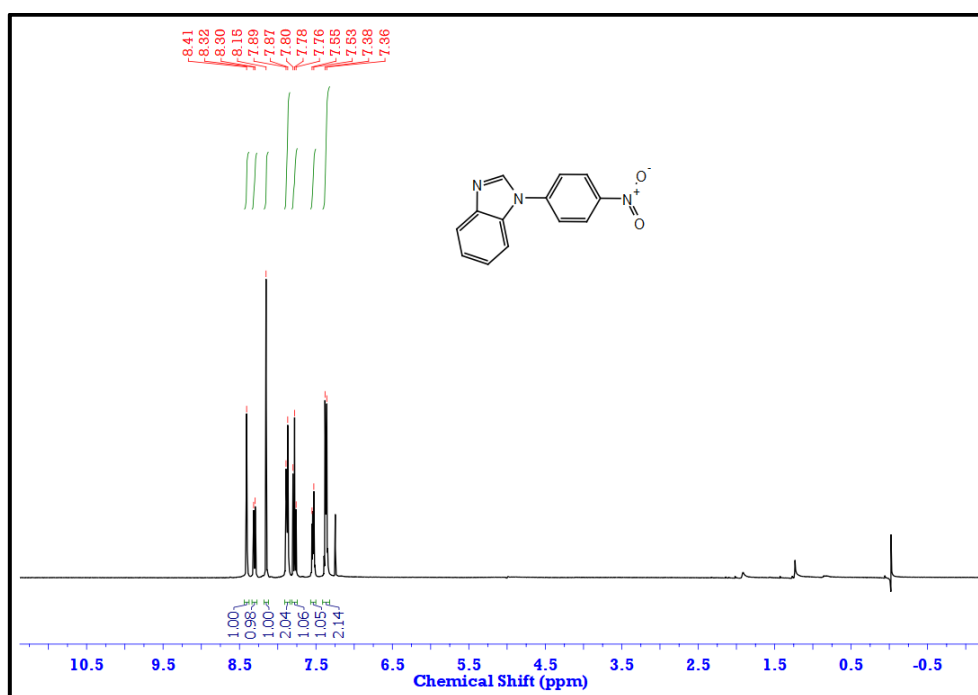


**Figure 5.14.** <sup>1</sup>H NMR Spectrum of 3o (1-(4-Nitrophenyl)-1*H*-benzo[*d*]imidazole) in CDCl<sub>3</sub>

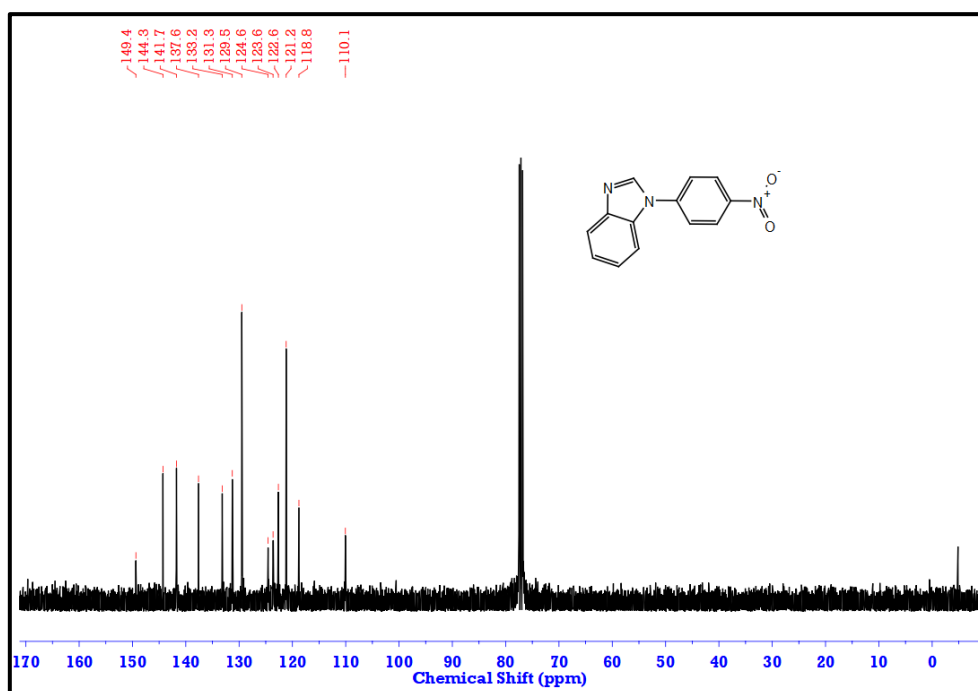


**Figure 5.15.** <sup>13</sup>C NMR Spectrum of 3o (1-(4-Nitrophenyl)-1*H*-benzo[*d*]imidazole) in CDCl<sub>3</sub>

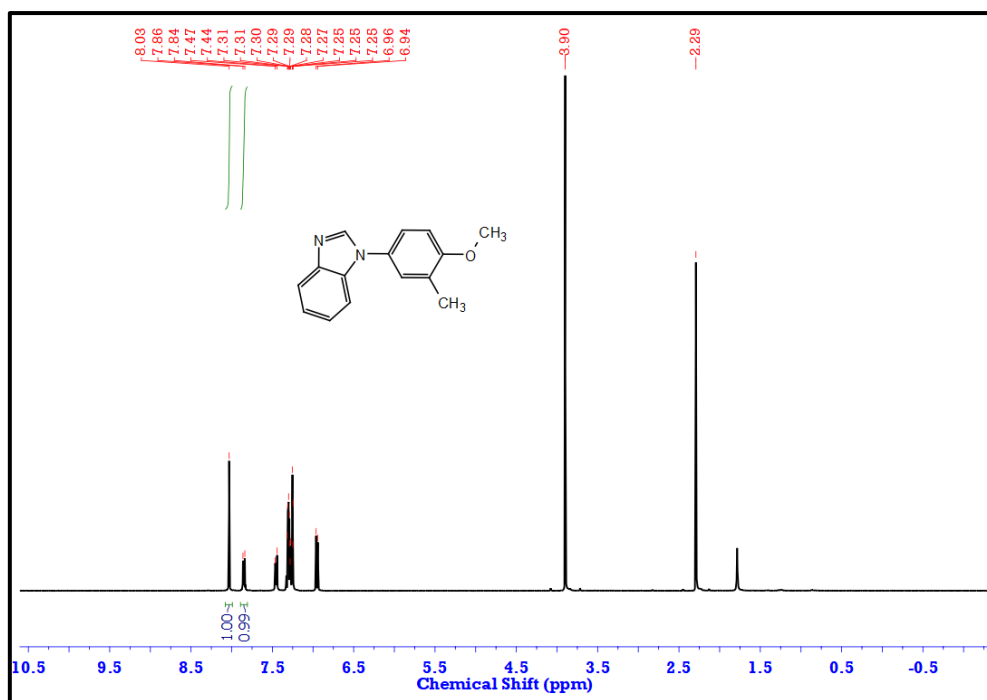


**Figure 5.16.** <sup>1</sup>H NMR Spectrum of 3q (1-(4-Methoxy-3-methylphenyl)-1H-benzo[d]imidazole in CDCl<sub>3</sub>)

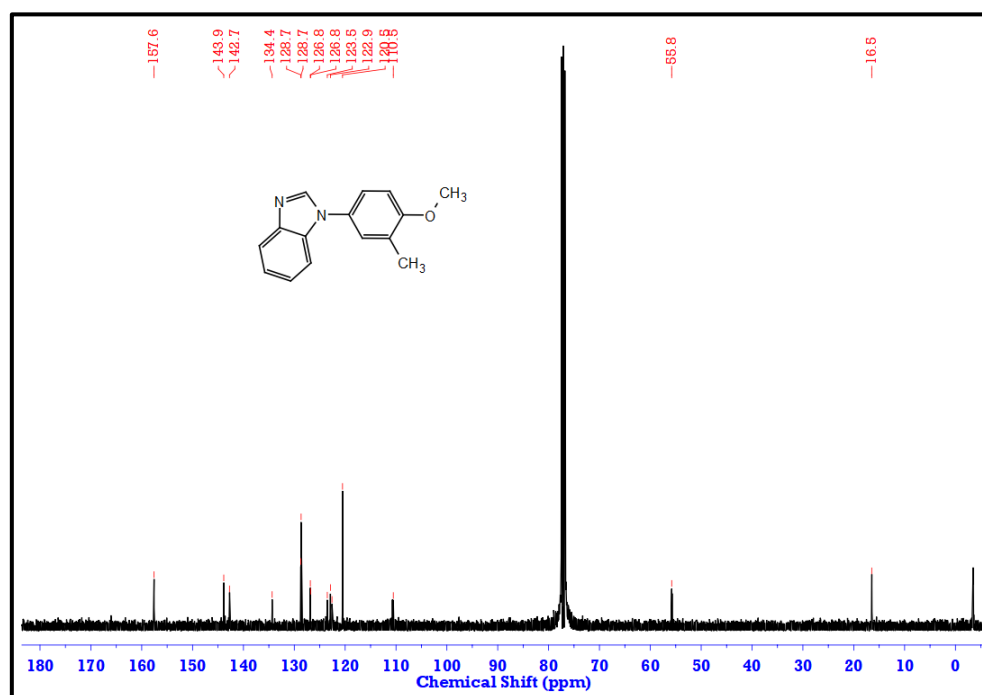


**Figure 5.17.** <sup>13</sup>C NMR Spectrum of 3q (1-(4-Methoxy-3-methylphenyl)-1H-benzo[d]imidazole in CDCl<sub>3</sub>)

### 5.7. Bibliography

- [1] Astruc, D. Introduction: nanoparticles in catalysis. *Chemical Reviews*, 120(2):461-463, 2020.
- [2] a) Khanna, P. K., Gaikwad, S., Adhyapak, P. V., Singh, N. and Marimuthu, R. Synthesis, and characterisation of copper nanoparticles. *Materials Letters*, 61(25):4711-4714, 2007; b) Dhas, N. A., Raj, C. P. and Gedanken, A. Synthesis, characterisation, and properties of metallic copper nanoparticles. *Chemistry of Materials*, 10(5):1446-1452, 1998; c) Usman, M. S., Zowalaty, M. E. E., Shameli, K., Zainuddin, N., Salama, M. and Ibrahim, N. A. Synthesis, characterisation, and antimicrobial properties of copper nanoparticles. *International journal of nanomedicine*, 2013:4467-4479, 2013.
- [3] Mott, D., Galkowski, J., Wang, L., Luo, J. and Zhong, C. J. Synthesis of size-controlled and shaped copper nanoparticles. *Langmuir*, 23(10):5740-5745, 2007.
- [4] a) Rajesh, K. M., Ajitha, B., Reddy, Y. A. K., Suneetha, Y. and Reddy, P. S. Synthesis of copper nanoparticles and role of pH on particle size control. *Materials Today: Proceedings*, 3(6):1985-1991, 2016; b) Park, B. K., Jeong, S., Kim, D., Moon, J., Lim, S. and Kim, J. S. Synthesis, and size control of monodisperse copper nanoparticles by polyol method. *Journal of Colloid and Interface Science*, 311(2):417-424, 2007; c) Aissa, M. A. B., Tremblay, B., Andrieux-Ledier, A., Maisonhaute, E., Raouafi, N. and Courty, A. Copper nanoparticles of well-controlled size and shape: a new advance in synthesis and self-organisation. *Nanoscale*, 7(7):3189-3195, 2015.
- [5] a) Lin, H. and Sun, D. Recent synthetic developments and applications of the ullmann reaction. A review. *Organic Preparations and Procedures International*, 45(5):341-394, 2013; b) Khan, F., Dlugosch, M., Liu, X. and Banwell, M. G. The palladium-catalysed Ullmann cross-coupling reaction: a modern variant on a time-honored process. *Accounts of Chemical Research*, 51(8):1784-1795, 2018; c) Akhtar, R., Zahoor, A. F., Irfan, M., Bokhari, T. H. and ul Haq, A., 2022. Recent green synthetic approaches toward Ullmann reaction: A review. *Chemical Papers*, 76(12):7275-7293, 2022.
- [6] a) Chinchilla, R. and Nájera, C. Recent advances in Sonogashira reactions. *Chemical Society Reviews*, 40(10):5084-5121, 2011; b) Karak, M., Barbosa, L. C. and Hargaden,

G. C. Recent mechanistic developments and next generation catalysts for the Sonogashira coupling reaction. *RSC Advances*, 4(96):53442-53466, 2014; c) Bakherad, M. Recent progress and current applications of Sonogashira coupling reaction in water. *Applied Organometallic Chemistry*, 27(3):125-140, 2013; d) Gazvoda, M., Virant, M., Pinter, B. and Košmrlj, J. Mechanism of copper-free Sonogashira reaction operates through palladium-palladium transmetallation. *Nature Communications*, 9(1):4814, 2018; e) Schilz, M. and Plenio, H. A guide to Sonogashira cross-coupling reactions: the influence of substituents in aryl bromides, acetylenes, and phosphines. *The Journal of Organic Chemistry*, 77(6):2798-2807, 2012.

[7] a) Gujral, S. S., Khatri, S., Riyal, P. and Gahlot, V. Suzuki cross coupling reaction-a review. *Indo Global Journal of Pharmaceutical Sciences*, 2(4):351-367, 2012.; b) Kotha, S., Lahiri, K. and Kashinath, D. Recent applications of the Suzuki–Miyaura cross-coupling reaction in organic synthesis. *Tetrahedron*, 58(48):9633-9695, 2002; c) Kadu, B. S. Suzuki–Miyaura cross coupling reaction: recent advancements in catalysis and organic synthesis. *Catalysis Science & Technology*, 11(4):1186-1221, 2021; d) Fihri, A., Bouhrara, M., Nekoueishahraki, B., Basset, J. M. and Polshettiwar, V. Nanocatalysts for Suzuki cross-coupling reactions. *Chemical Society Reviews*, 40(10):5181-5203, 2011.

[8] a) Heravi, M. M., Kheilkordi, Z., Zadsirjan, V., Heydari, M. and Malmir, M. Buchwald-Hartwig reaction: an overview. *Journal of Organometallic Chemistry*, 861:17-104, 2018; b) Dorel, R., Grugel, C. P. and Haydl, A. M. The Buchwald–Hartwig amination after 25 years. *Angewandte Chemie International Edition*, 58(48):17118-17129, 2019; c) Takale, B. S., Kong, F. Y. and Thakore, R. R., 2022. Recent Applications of Pd-Catalysed Suzuki–Miyaura and Buchwald–Hartwig Couplings in Pharmaceutical Process Chemistry. *Organics*, 3(1):1-21, 2022.

[9] a) Devi, P. S., Saranya, S. and Anilkumar, G. Recent advances in Chan-Lam Coupling Reaction. *Catalysis Science & Technology*, 14, 2320-2351; b) Abedinifar, F., Mahdavi, M., Rezaei, E. B., Asadi, M. and Larijani, B. Recent developments in arylation of N-nucleophiles via Chan-Lam reaction: updates from 2012 onwards. *Current Organic Synthesis*, 19(1):16-30, 2022; c) Chen, J. Q., Li, J. H. and Dong, Z. B. A review on the latest progress of Chan-Lam coupling reaction. *Advanced Synthesis &*



*Catalysis*, 362(16):3311-3331, 2020; d) Vijayan, A., Rao, D. N., Radhakrishnan, K. V., Lam, P. Y. and Das, P. Advances in carbon–element bond construction under Chan–Lam cross-coupling conditions: a second decade. *Synthesis*, 53(05):805-847, 2021.

[10] a) Bagheri, H. and Baharfar, R. Magnetic MCR-Functionalised Graphene Oxide Complexed with Copper Nano-Particles: An Efficient and Recyclable Nanocatalyst for Ullmann C–N Coupling Reaction. *Polycyclic Aromatic Compounds*, 43(8):7580-7596, 2023; b) Dubey, A.V. and Kumar, A.V. A Bio-Inspired Magnetically Recoverable Palladium Nanocatalyst for the Ullmann Coupling reaction of Aryl halides and Arylboronic acids In Aqueous Media. *Applied Organometallic Chemistry*, 34(5):e5570, 2020.

[11] Anand, M. and Nørskov, J. K. Scaling relations in homogeneous catalysis: analysing the Buchwald–Hartwig amination reaction. *ACS Catalysis*, 10(1):336-345, 2019.

[12] Falß, S., Tomaiuolo, G., Perazzo, A., Hodgson, P., Yaseneva, P., Zakrzewski, J., Guido, S., Lapkin, A., Woodward, R. and Meadows, R. E. A continuous process for Buchwald–Hartwig amination at micro-, lab-, and mesoscale using a novel reactor concept. *Organic Process Research & Development*, 20(2):558-567, 2016.

[13] Liu, Y., Prashad, M. and Shieh, W. C. A Scalable Synthesis of an Atropisomeric Drug Substance *via* Buchwald–Hartwig Amination and Bruylants Reactions. *Organic Process Research & Development*, 18(1):239-245, 2014.

[14] Sperry, J. B., Price Wiglesworth, K. E., Edmonds, I., Fiore, P., Boyles, D. C., Damon, D. B., Dorow, R. L., Piatnitski Chekler, E. L., Langille, J. and Coe, J. W. Kiloscale Buchwald–Hartwig Amination: Optimised Coupling of Base-Sensitive 6-Bromoisquinoline-1-carbonitrile with (*S*)-3-Amino-2-methylpropan-1-ol. *Organic Process Research & Development*, 18(12):1752-1758, 2014.

[15] Liori, A. A., Stamatopoulos, I. K., Papastavrou, A. T., Pinaka, A. and Vougioukalakis, G. C. A Sustainable, User-Friendly Protocol for the Pd-Free Sonogashira Coupling Reaction. *European Journal of Organic Chemistry*, 2018(44):6134-6139, 2018.

- [16] Lam, P. Y., Clark, C. G., Saubern, S., Adams, J., Winters, M. P., Chan, D. M. and Combs, A. New aryl/heteroaryl C-N bond cross-coupling reactions *via* arylboronic acid/cupric acetate arylation. *Tetrahedron Letters*, 39(19):2941-2944, 1998.
- [17] Cundy, D. J. and Forsyth, S. A. Cupric acetate mediated N-arylation by arylboronic acids: A preliminary investigation into the scope of application. *Tetrahedron letters*, 39(43):7979-7982, 1998.
- [18] Sun W., Gao L., Sun X., Zheng G. A novel route with a Cu(ii)-MOF derived structure to synthesise Cu/Cu<sub>2</sub>O NPs@ graphene: the electron transfer leads to the synergistic effect of the Cu(0)-Cu(I) phase for an effective catalysis of the Sonogashira cross-coupling reactions. *Dalton Transactions*, 47(16):5538-5541, 2018.
- [19] Kar A. K., Srivastava R. Selective synthesis of Cu-Cu<sub>2</sub>O/C and CuO-Cu<sub>2</sub>O/C catalysts for Pd-free C-C, C-N coupling and oxidation reactions. *Inorganic Chemistry Frontiers*, 6(2):576-589, 2019.
- [20] Fors B. P., Davis N. R., Buchwald S. L. An Efficient Process for Pd-Catalysed C-N Cross-Coupling Reactions of Aryl Iodides: Insight into Controlling Factors. *Journal of the American Chemical Society*, 131(16):5766-5768, 2009.
- [21] Kou J., Saha A., Bennett-Stamper C., Varma R. S. Inside-out core-shell architecture: controllable fabrication of Cu<sub>2</sub>O@Cu with high activity for the Sonogashira coupling reaction. *Chemical Communications*, 48(47):5862-5864, 2012.
- [22] Mathey, Y., Greig, D. R. and Shriver, D. F., 1982. Variable-temperature Raman and infrared spectra of the copper acetate dimer Cu<sub>2</sub>(O<sub>2</sub>CCH<sub>3</sub>)<sub>4</sub>(H<sub>2</sub>O)<sub>2</sub> and its derivatives. *Inorganic Chemistry*, 21(9):3409-3413, 1982.